Medical Engineering & Physics 33 (2011) 832–839

Contents lists available at ScienceDirect

Medical Engineering & Physics

journal homepage: www.elsevier.com/locate/medengphy

Modelling wall shear stress in small arteries using the Lattice Boltzmann method: influence of the endothelial wall profile

Giuseppe Pontrelli[a,*], Carola S. König[b], Ian Halliday[c], Timothy J. Spencer[c], Michael W. Collins[d], Quan Long[b,d], Sauro Succi[a]

[a] Institute for Applied Computing, National Research Council (IAC-CNR), Italy
[b] Institute for Bioengineering, Brunel University, London, UK
[c] Materials and Engineering Research Institute, Sheffield Hallam University, Sheffield, UK
[d] School of Engineering and Design, Brunel University, London, UK

ARTICLE INFO

Article history:
Received 20 January 2010
Received in revised form 21 March 2011
Accepted 23 March 2011

Keywords:
Arterial endothelium
Blood flow
Wall shear stress
Lattice Boltzmann methods
LBM

ABSTRACT

In order to address the problem of blood flow over the endothelium in small arteries, the near-endothelial region is here studied in more detail. The method used is a finite-volume discretisation of a Lattice Boltzmann equation over unstructured grids, named unstructured Lattice Boltzmann equation (ULBE). It is a new scheme based on the idea of placing the unknown fields at the nodes of the mesh and evolving them based on the fluxes crossing the surfaces of the corresponding control volumes. The study shows a significant variation and a high sensitivity of wall shear stress to the height of the endothelium corrugation and the presence of erythrocytes. The latter were modelled as deformable, viscous particles within a fluid continuum.

© 2011 IPEM. Published by Elsevier Ltd. All rights reserved.

1. Introduction

The flow of blood in arteries induces a viscous drag between the outermost laminae of the fluid and the vessel wall. This mechanism has a potential impact on the pathogenesis of arterial diseases. The shear stress imposed on the wall can affect the functional and structural integrity of the endothelial cells (EC's), and the possibility that such effects might be related to the development of atherosclerosis has stimulated a great deal of investigation [1,2]. Stretching of EC's may modify the properties of the cell's membrane in the form of its permeability and receptors. Lesions usually occur at specific points of the arterial tree, which suggests that differences in local stress may play some role in its initialization. It is now commonly accepted that the preferred occurrence of atherosclerosis is in low wall shear regions, and variation of wall shear stress is playing a key role in the development of aneurysms, even in medium sized arteries [3]. Already early work by Caro et al. [4] observed that "From our own observations, and those of others, we show that the distribution of early atheroma in man is coincident with those regions in which arterial wall shear rate is expected to be relatively low, while the development of lesions is inhibited or retarded in those regions in which wall shear rate is expected to be relatively high". Malek et al. [5] link atherosclerotic-prone sites to low shear stress <0.4 Pa and above 1.5 Pa with an atheroprotective gene expression profile. Sato and Ohashi give the range of EC shear stress exposure as varying from 1 to 4 Pa in large arteries [6]. Recently, Punchard et al. show that *in vitro* monolayer EC's have a dysfunctional response to low wall shear stress (0.5 Pa) as observed by gene expression [7]. While wall shear stress is now unanimously accepted as a key factor in endothelial response and atherogenesis in large arteries, detailed study of the near-wall region, with the exception of Ref. [8], is lacking. However, this becomes particularly necessary in the case of small arteries, where the endothelial surface layer (ESL) is more prominent.

Several studies concerning flows over wavy walled boundaries, both from analytical [9,10], numerical [11–13] and experimental [14] points of view have been carried out. These studies are based on a regular pattern of the wall profile, say sinusoidal or arc-shaped with different amplitudes, and use perturbation analysis. Most are concerned with relatively moderate and high Reynolds numbers and aim to understand transition from laminar to turbulent flow, by evidencing the formation of vortices and flow separation. In [15] the characteristics of mass transfer are studied in relation to the onset of turbulence.

In this study, though, we consider the undulation of the wall as a sequence of EC's with their dimension as obtained from the literature (Fig. 1). Only recently it has been recognized that the endothelial glycocalyx may contribute to the protection of the vas-

* Corresponding author. Tel.: +39 0649270927; fax: +39 064404306.
E-mail address: giuseppe.pontrelli@gmail.com (G. Pontrelli).

1350-4533/$ – see front matter © 2011 IPEM. Published by Elsevier Ltd. All rights reserved.
doi:10.1016/j.medengphy.2011.03.009

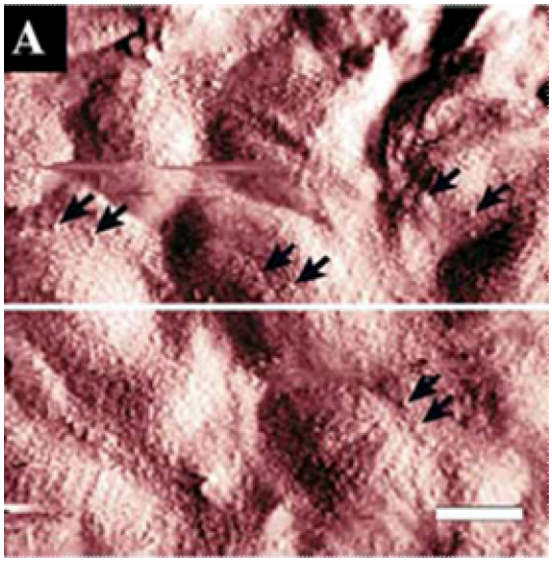

Fig. 1. The rough surface of the endothelium (from Ref. [28]). Arrows point to granular structures on EC's surface, white line marks scanning line for height profile evaluation, scale bar corresponds to 5 μm.

cular wall in small vessels against disease by reducing friction to the flow of blood and serving as a barrier for loss of fluid through the vessel wall. In times of inflammation, though, the endothelial layer may be sheared off, exposing the 'bare surface' of the wavy endothelium. This allows leukocytes to be attached to the surface and facilitates the transfer of plasma across the vessel wall into the underlying structure [16]. In this work, however, only mechanical effects are considered, while all chemical and biological processes of the endothelium are neglected. The haemodynamic problem is solved by using a Lattice Boltzmann (LB) approach [17]. The main advantages of LB are its simplicity and amenability to parallel computing [18–20]. With due implementation effort, high parallel efficiency can be preserved also in image-based geometries exhibiting real-life complexity [21–23]. In particular, owing to its kinetic nature, the pressure field and the stress tensor are locally available, without the need of solving any (usually expensive) Poisson problem.

Another key property of LB is that non-linearities are local, manifesting in a quadratic dependence of the local equilibrium on the flow field, and the non-localities are linear, because advection proceeds along constant, straight lines defined by the discrete speeds. This is a very useful property, not shared by the Navier–Stokes equations, in which non-linearity and non-locality come together into the same convective term, that is, the fluid moves its own momentum along a space-time changing direction defined by the flow speed itself. However, a recognized weakness of LB is its restriction to regular, uniform lattices (Cartesian grids). This limitation is particularly severe whenever high local resolution is required, as is the case for most flows of biomedical interest. For instance, curved boundaries must be approximated by staircase profiles aligned with the gridline coordinates, an approximation which can lead to severe inaccuracies, unless a sophisticated treatment of the boundary is devised or high grid resolution applied [24]. The problem has motivated a wide body of research aimed at extending the LB method to non-uniform grids with boundary conditions capable of accommodating curved boundaries [25]. Particularly interesting are the recent attempts to formulate LB on fully unstructured grids using cell-vertex finite-volume schemes [26] and its extension to non-Newtonian flows [27].

2. Formulation of the problem

In nearly all studies of haemodynamics in arteries, blood is assumed to be an incompressible, Newtonian fluid, the arterial wall to be smooth, being the sub-micrometric corrugations neglected and the endothelium surface considered flat: this does not imply a significant variation in the flow field, but it can be relevant in computing WSS, which is constant in a flat-walled artery. Indeed, the internal surface of the vessel wall is covered by EC's that form a continuous, wavy layer. We assume that the EC membrane is solid-like, so the cells keep their shape while subjected to the shear stress due to the blood stream. An EC has been estimated to be about 15 μm long by 0.5 μm high [28] (see Fig. 1). We consider a two-dimensional channel flow between two boundary surfaces located at $y = \pm h(x)$, with the x-axis in the direction of the mean flow. The shape of each internal wall appears as a smoothly corrugated surface: the channel semi-width is obtained as a perturbation around a reference value H:

$$h(x) = H \pm \delta(x) = H(1 \pm \varepsilon)$$

where $\delta(x)$ is given by repeating the profile of a single EC several times and subsequently smoothing it [29]. In the above equation $\varepsilon = \delta/H$ represents the corrugation degree.

Although the wall surface is, in reality, constituted by an irregular (randomly rough) sequence of ECs, for simplicity we assume that they are regularly aligned and equally distributed over both upper and lower walls, and that their size is independent of the channel semi-width, H. For all H, the aspect ratio of the channel has been fixed at 3, unless otherwise stated.

The aim of this work is to investigate the dependence and the sensitivity of the WSS to the wall roughness and the corrugation height, and to quantify the WSS differences with the variation of vessel diameter and flow rates. Assuming axi-symmetry, this study is limited to a two-dimensional straight channel, where a Newtonian fluid of viscosity μ and density ρ flows, being driven by a force (pressure difference) which is constant over the cross-sectional area. Due to the absence of secondary flows, the fluid dynamics predictions are based on a steady case, on the assumption that the mean flow in pulsatile conditions is similar to steady flow with the same time averaged velocity. On the other hand, the importance of pulsatility reduces with reducing vessel diameter [30]. As blood is not, strictly speaking, a continuous fluid, we proceed briefly to examine, in Section 6, the extent to which WSS may further vary due to its true nature as a dense particulate suspension.

3. Lattice Boltzmann methodology

Let us consider the classical differential form of the single-time relaxation Lattice Boltzmann equation:

$$\partial_t f_i + \vec{c}_i \cdot \nabla f_i = -\omega\,(f_i - f_i^{eq}) + F_i \tag{1}$$

The above equation models hydrodynamic fluid flow by tracking the time-evolution of the density distribution function of pseudo-particles (or populations), defined as $f_i(\vec{x}, t) \equiv f(x, \vec{v} = \vec{c}_i, t)$, where f_i is the probability of finding a particle at site $\vec{x}$, at time t moving along the lattice direction defined by the discrete speed $\vec{c}_i$. In Eq. (1) F_i represents the effect of external/internal sources of mass/momentum/energy. The left-hand side of Eq. (1) represents the particle free-streaming, whereas the right-hand side represents molecular collisions via a single-time relaxation towards local equilibrium f_i^{eq} on a typical timescale $1/\omega$ [31]. The local equilibrium is the Maxwell–Boltzmann distribution function expanded second order in the local Mach number:

$$f_i^{eq} = \rho w_i \left[1 + \beta u_i + \frac{\beta^2}{2}(u_i^2 - u^2)\right] \tag{2}$$

where $\beta = 1/c_s^2$, being c_s the lattice sound speed, $\rho = \sum_i f_i$ the fluid density, $\vec{u} = \sum_i \vec{c}_i f_i/\rho$ is the fluid speed and w_i are weight coefficients (normalized to unity) associated with zero-flow global equilibriums. In the limit of weak departures from local equilibrium, i.e. small Knudsen numbers, it can be shown through a Chapman–Enskog analysis that the discrete LB recovers the dynamic behaviour of a fluid with pressure $p = \rho c_s^2$ and kinematic viscosity $\nu = c_s^2((1/\omega) + k\Delta t)$, where k is a numerical coefficient depending on the specific time-marching scheme ($k = 0$ in the continuum time limit, and $k = -1/2$ for the standard LB equation on uniform Cartesian grids [31]).

In order to recover the correct fluid dynamic equations in the macroscopic limit, the set of discrete speeds must satisfy mass, momentum and energy conservation, as well as rotational symmetry. It should be noted that only a limited class of lattices exhibits the right symmetry to ensure the conservation constraints. In the present work we shall refer to the two-dimensional nine-speed model (known as D2Q9) defined by the following set of discrete speeds:

$$\vec{c}_0 = (0,0), \quad \vec{c}_1 = (1,0), \quad \vec{c}_2 = (0,1),$$
$$\vec{c}_3 = (-1,0), \quad \vec{c}_4 = (0,-1), \quad \vec{c}_5 = (1,1),$$
$$\vec{c}_6 = (-1,1), \quad \vec{c}_7 = (-1,-1), \quad \vec{c}_8 = (1,-1).$$

with weights $w_0 = 4/9$, $w_{1-4} = 1/9$, $w_{5-8} = 1/36$ in Eq. (2). The aforementioned low-Mach number expansion restricts the use of the discrete Boltzmann equation to quasi-incompressible flows, with negligible space-time variation of the fluid density. On the other hand, since the discrete LB fluid obeys an ideal equation of state, significant pressure drops can only be sustained by supplementing/replacing the pressure gradient with an external body force (force per unit volume), $\vec{F}$. In a steady plane-channel flow, the magnitude of the body force is determined by imposing an exact balance with dissipative effects, i.e. $F = \mu \partial_{yy} u_x$. This delivers:

$$F = \frac{2\mu U_{\max}}{H^2}.$$

This approach is equivalent to assign a pressure gradient $G = 2\mu U_{\max}/H^2$ along the channel length. The effect of the body force on the discrete populations in Eq. (1) is given by:

$$F_i = \frac{w_i \vec{F} \cdot \vec{c}_i}{c_s^2}$$

which finally results in the following forcing term:

$$F_i = \frac{2U_{\max}}{\omega H^2} \tag{3}$$

Boundary conditions are no-slip at top/bottom walls and periodic at inlet/outlet.

4. LB on unstructured grids

The presented standard LB method is macroscopically similar to a uniform Cartesian-grid solver, and this represents a severe limitation for solving complex geometries typical of haemodynamic flows. To overcome this drawback, the classical LB method has been extended to use irregular grids. This approach is based on a finite-volume scheme of the cell-vertex type consisting of a tessellation based on triangular elements. The use of unstructured grids with control volumes of arbitrary polygonal shape allows local grid refinements which are not possible with the standard LB. To solve Eq. (1), the nine discrete populations $f_i(\vec{x}, t)$ associated to each node P of the discrete grid (Fig. 2) represent the unknowns of the problem. The finite volume over which Eq. (1) is integrated is defined by means of the set of K triangles, which share P as a common vertex. Since the discrete grid is unstructured, each node is identified by its coordinates and the connectivity (P,P_k,P_{k+1}) is free to change from node to node. As shown in Fig. 2, the portion of the control volume $\Omega_k = [C_k, E_k, P, E_{k+1}]$ that refers to the k-th triangular element is built through the union of the two sub-grid triangles $\Omega_k^- = [P, E_k, C_k]$ and $\Omega_k^+ = [P, C_k, E_{k+1}]$, where C_k is the centre of the grid element and E_k and E_{k+1} are the midpoints of the edges that share P as a common vertex. Populations at off-grid points E_k and C_k are calculated with standard linear interpolations. Application of the Gauss theorem to each finite volume portion yields the following set of ordinary differential equations:

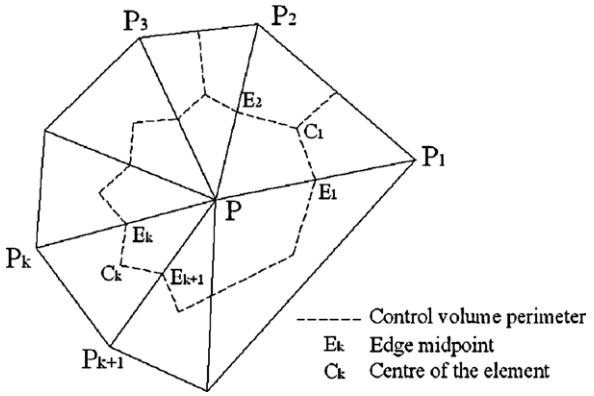

Fig. 2. The cell-vertex finite-volume discretisation around a grid point P.

$$\partial_t f_i(P,t) = \frac{1}{V_P} \sum_k (\Phi_{ik} - \Xi_{ik}) \tag{4}$$

where the sum $k = 0, K$ runs over the control volume $\Omega_P = \bigcup_k \Omega_k$ obtained by joining the centres C_k with edge midpoints E_k, V_P is the volume of Ω_P and the index $k = 0$ denotes the pivotal point P. Finally, Φ_{ik} denote the fluxes associated with the streaming operator and Ξ_{ik} the integral of the collision operators of the i-th population at the k-th node, respectively. The detailed expressions of the streaming and collision matrices S_{ik} and C_{ik} give the following general form of the Unstructured Lattice Boltzmann Equation (ULBE):

$$\partial_t f_i(P,t) = \sum_{k=0}^{K} S_{ik} f_i(P_k,t) - \omega \sum_{k=0}^{K} C_{ik} [f_i(P_k,t) - f_i^{eq}(P_k,t)]$$

and they obey to the following sum rules [26]:

$$\sum_{k=0}^{K} S_{ik} = 0, \qquad \sum_{k=0}^{K} C_{ik} = 1 \quad \forall i$$

It is readily checked that the stress tensor $\Pi_{\alpha\beta}$ is related to the non-equilibrium component of the momentum flux tensor by the following *local* expression:

$$\Pi\alpha\beta = \sum_i (f_i - f_i^{eq}) c_{i\alpha} c_{i\beta}$$

where α, β run over spatial dimensions.

Boundary conditions for ULBE need to cope with the fact that the corresponding control volumes do not close up, leaving two external edges exposed on the boundary. To date, the best strategy to deal with this problem is provided by the so-called *covolume method*. Within this method, the boundary nodes are treated exactly as fluid nodes, the only difference being that the edge fluxes are evaluated explicitly by using interpolation at the boundary edges. The boundary condition is then given in terms of enforced macroscopic values in the equilibrium distribution function ($U = 0$ for the no-slip boundary condition). The covolume method works

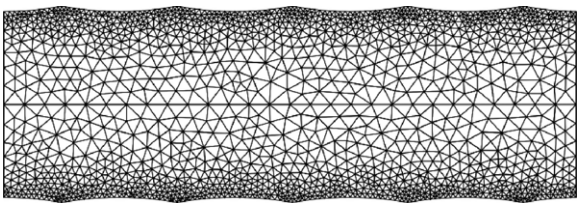

Fig. 3. The 2D arterial segment (diameter 25 μm) covered by a refined triangular mesh.

for generic boundary geometries and has proven to support relatively strong boundary gradients [26].

5. Computational results

First of all, a benchmark test was intended to assess the efficacy of the ULBE methodology on a flat-walled artery fully developed flow model. We considered a uniform unstructured automatically generated grid on a 2D channel $[-3H,3H]\times[-H,H]$, consisting of 5634 equidistributed elements, and the simulations were performed for a wide range of Reynolds numbers. A comparison of ULBE solution with the Poiseuille velocity profile:

$$u(y) = U_{\max}\left(1 - \frac{y^2}{H^2}\right) \tag{5}$$

exhibits a maximum, non-dimensional error of $E \simeq 10^{-5}$, while the discrepancy with the wall shear stress

$$\tau = \frac{4\mu U_{\max}}{D} \tag{6}$$

results of $E \simeq 10^{-4}$. Other benchmark tests on ULBE method and its extension to shear-thinning flows have been recently carried out [27]. Typical values for arterioles (microcirculation) are:

$$\rho = 1\,\mathrm{g/cm^3} \qquad \mu = 0.027P$$
$$D = 2H = 25\text{–}150\,\mu\mathrm{m} \qquad U_{\max} = 1\text{–}40\,\mathrm{cm/s}$$

that combine in a range of $\mathrm{Re} = \rho D U_{\max}/\mu \cong 0.1\text{–}20$. Although these values can be larger than those pertaining to the arterioles, this numerical set is aimed to understand the flow dependence on the geometrical-physical parameters on a wider range and, in particular, the sensitivity of the solution on the degree of corrugation ε and on the Reynolds number.

The COMSOL package was used to generate the grid, with a mesh refinement near the wall to suit the wavy profile. For this case, the grid size ranges from 3830 ($D = 25$) to 7960 ($D = 150$) triangular elements. The grid is refined near the wall to suit the wavy endothelial surface (Fig. 3). The channel maximum semi-width is normalized to $H = 1$. The time step Δt is chosen in relation to the smallest grid size (which typically reduces as H increases) in order to satisfy the CFL condition.

At such small Reynolds number the velocity profiles preserve the parabolic shape (Fig. 4), but the wall corrugation causes a local change of the velocity derivative and hence an oscillation on the WSS values. As Fig. 5 shows, the stress rises linearly in the transverse direction, except near the wall. Here the variation in cross-sectional width generates a substantial local difference in the shear rates and stresses. Fig. 5 shows that the consequence is a local variation of these quantities in a boundary layer close to the wall and an oscillation of the shear rates and WSS along the endothelium.

As expected, an increase in the maximum shear stress, τ_+ with velocity, U is observed along the endothelium. Fig. 6 shows that τ_+ increases essentially linearly with velocity, but inversely with D; this is consistent with Eq. (6). A similar behaviour holds for τ_-. As

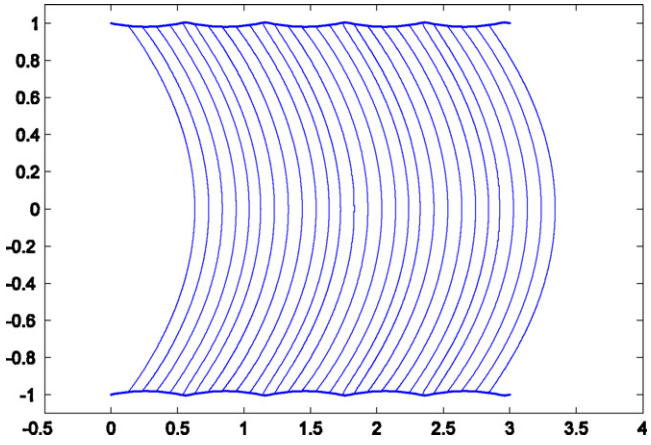

Fig. 4. Parabolic velocity profiles (×100) along the wavy-walled channel ($U = 40$ cm/s, $D = 50$ μm).

a consequence, WSS oscillates between a minimum τ_- and maximum τ_+ values, which match the undulation of the wall, that is, in the studied low Reynolds number regime, the minimum and maximum of τ correspond to the maximum and minimum diameters, respectively.

Their values depend on the diameter and flow rate, but their ratio τ_-/τ_+ remains almost constant (Table 1), though numerical instabilities, which can be attributed to the grid discreteness near the wavy wall, are present in the WSS values and are bound within a few percent. Because it is argued that the amplitude of the time-dependent fluctuating WSS can play a relevant role in the formation and development of atherosclerotic diseases we also investigated the question of geometry dependency. In the next section an analysis of this is carried out. In Fig. 7, τ_+ and τ_- are shown as a function of the corrugation degree ε. In the absence of experimental data specifically for arterioles the limiting conditions used were those for large arteries given in [6]. We would expect the two conditions of high and low shear stress to be similarly detrimental in small arteries. The trend shown for both, τ_+ and τ_- is not unexpectedly linear.

In agreement with previous studies [10,11], at such low Reynolds ($\mathrm{Re} < 25$) and with moderate wall corrugation, we are under the critical regime to be attained for the flow separation and the flow remains laminar.

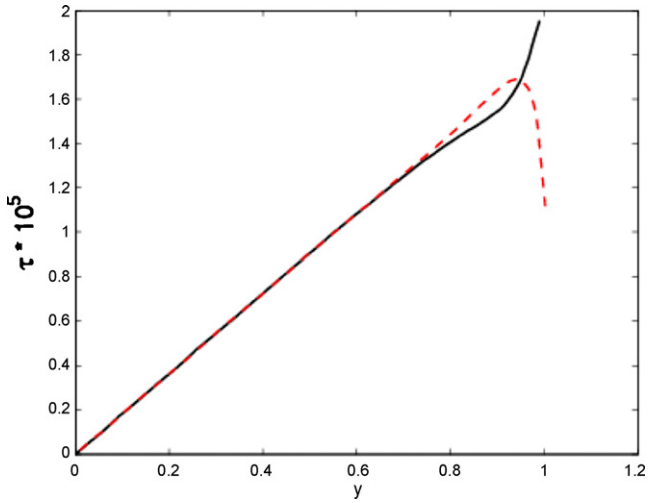

Fig. 5. Cross-stream variation of shear stress: continuous line – peak of EC; dashed line – valley of EC (LB units).

Table 1
The ratio τ_-/τ_+ at different velocities (cm/s) and diameters (μm). The corresponding Reynolds numbers are bracketed.

	$D=25$	$D=50$	$D=100$	$D=150$
$U=1$	0.55 (0.09)	0.54–0.55 (0.185)	0.55–0.56 (0.37)	0.55–0.57 (0.55)
$U=20$	0.55 (1.85)	0.54–0.55 (3.7)	0.55–0.56 (7.4)	0.55–0.57 (11.11)
$U=40$	0.55 (3.7)	0.54–0.55 (7.4)	0.55–0.56 (14.81)	0.55–0.57 (22.22)

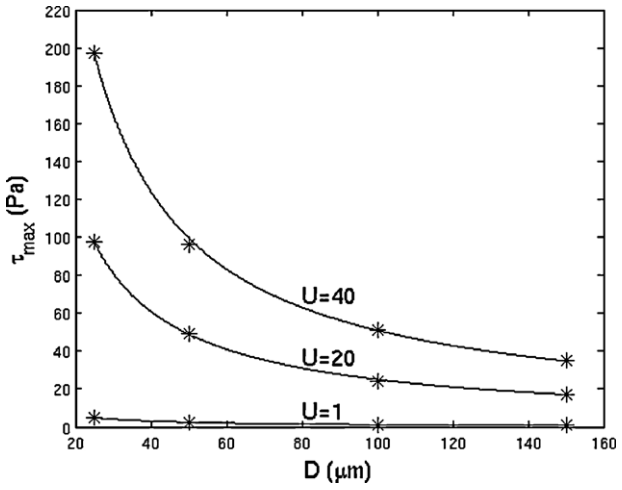

Fig. 6. Variation of the maximum wall shear stress profile for varying diameter for various maximum inlet velocities (cm/s). Stars indicate results from simulations, continuous lines are fitting curves.

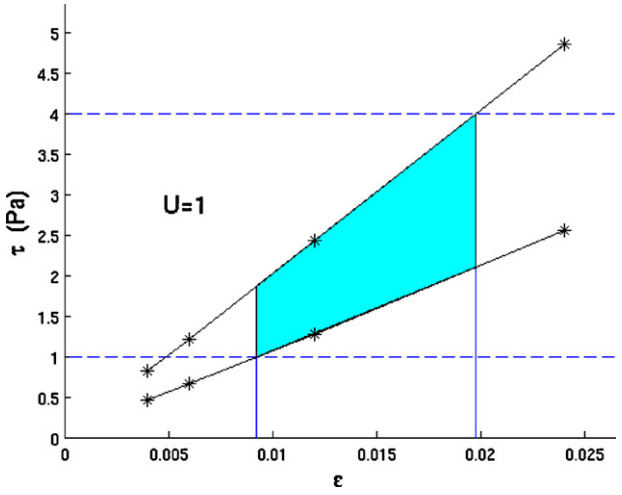

Fig. 7. Linear rise of τ_- and τ_+ as a function of corrugation degree ε for the case of $U_{max}=1$ cm/s. The region between 4 and 1 Pa shows the typical range of WSS in large arteries [6].

Tables 2 and 3 show the spatial amplitude of the oscillation $A=(\tau_+-\tau_-)/2$ and demonstrate the (almost) linear increase with D. The ratio of the amplitude over the corresponding straight wall value τ^* is nearly 25% in all cases. The results show a marked variation of τ with the diameter, which increases for smaller sized arteries. Although the wall corrugation does not influence the flow pattern notably, it induces a significant variation in τ.

6. WSS variation due to the particulate nature of blood

The preceding section investigates in detail the WSS behaviour of blood approximated as an incompressible Newtonian fluid with a realistic EC or "wavy" wall boundary conditions. In reality, blood is a complex particulate fluid in which an incompressible Newtonian plasma advects deformable erythrocytes. As a consequence, spatial-temporal WSS fluctuations must occur. A detailed study of such WSS effects is beyond the scope of the current article but some evaluation is called-for, to estimate the particulate influence.

Models of the motion of a single erythrocyte with an elastic membrane and restricted deformation in non-uniform capillaries, as presented by Secomb and Hsu [32] have been extended to account for a deformable ESL. It was found that this deformable ESL will reduce the impact of irregularity on flow resistance and, possibly, protect RBC's from damage from fluctuating stresses [33]. Also, many deformable erythrocytes have been modelled in uniform capillaries with LBM [34,35]. Clearly, a flow in which particles are free to redistribute themselves cannot be described as steady, even when its short-time averaged external driving conditions are constant. Furthermore, the structure of the WSS fluctuations must vary with hematocrit, Re and geometry, even in smooth vessels [34].

In this section we confine ourselves to assessing the statistics of particulate-induced WSS fluctuations in a system closely related to that studied in the previous section which, we argue below, allows for simpler models of elasticity. Restricting hematocrit further justifies the use of less demanding LBM models, which are more accurate in other respects, as is explained below.

We consider an axially symmetric system containing, in terms of Fig. 3, only five erythrocytes, all equally-spaced in the axial direction, one per spatial wall wavelength. The latter, denoted λ, was chosen to be $\lambda=15$ μm and, to reduce computational overhead, the total channel height was reduced to $H=2\lambda/3=10$ μm. There is, therefore, one or zero erythrocyte(s) at a given axial location, at any instant. Each erythrocyte was modelled as a deformable, viscous drop with appropriate kinematic viscosity contrast (increase factor of 7), advecting under the influence of a specified axial pressure gradient. A multi-component LB method [36] was used to represent the deformable particles, along with an appropriate sub-grid "continuous bounce-back" representation for the wavy walls [37]. Flow was driven by a specified pressure difference, applied across the vertical system boundaries [38]. To represent erythrocytes, the initial, undeformed, drop radius should approximate one third to one half of the wavy walls' wavelength, λ. We chose an initial drop diameter of $\lambda/3$ (and an initial spherical shape), resulting in an effective two-

Table 2
The spatial amplitude of oscillation of τ and its ratio to the corresponding flat-walled value τ^* at $U_{max}=1$ cm/s and at several diameters.

D (μm)	$\varepsilon=\delta/H$	A (Pa)	A/τ^*
150	0.0067	0.177	0.24
100	0.01	0.272	0.25
50	0.02	0.576	0.26
25	0.04	1.152	0.26

Table 3
The spatial amplitude of oscillation of τ and its ratio to the corresponding flat-walled value τ^* at $U_{max}=20$ cm/s and at several diameters.

D (μm)	$\varepsilon=\delta/H$	A (Pa)	A/τ^*
150	0.0067	3.733	0.25
100	0.01	5.52	0.25
50	0.02	11.2	0.25
25	0.04	21.76	0.25

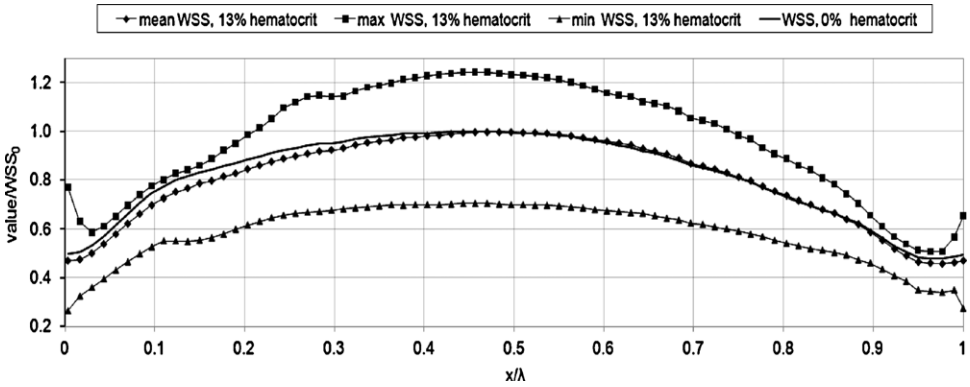

Fig. 8. The measured temporal maximum, minimum and mean WSS values, for 13% hematocrit, normalized to the spatial-temporal maximum, WSS_0, measured at 0% hematocrit (i.e. with only the plasma fluid component present in the multi-component LBE system) for all spatial positions on the wavy wall. For reference, the broken line *without markers* corresponds to the steady WSS at 0% hematocrit. The small irregularities at certain values of x/λ result from a small artefact associated with the LBE lattice closure.

dimensional hematocrit given by $\pi(\lambda/6)^2/2\lambda(\lambda/3) = \pi/24$, which is close to 13%.

Previous LBM based computational modelling of multiple, explicitly represented erythrocytes in plasma represents the latter as elastic Dirichlet boundaries of conserved area, which are deformed and advected by flow stresses [34,35]. Such models are unnecessary in the present context, given that hematocrit and associated volume exclusion effects, Reynolds number and particle deformation are all small. Further, problems arise in LBM with solid Lagrangian particulates, for lattice sites cross moving boundaries, enter the flow domain and therefore require initialization, which process can result in instabilities. The relatively simple immiscible drop algorithm employed in here is free of such problems, its hydrodynamics is physically accurate (in the contact region, this means that our drop model recovers kinematic and dynamic conditions from which we derive the lubrication and squeeze flow dynamics essential in portraying the EC-particulate contact: see [39] and references therein) and it automatically returns constraints of volume conservation and exclusion. However, the erythrocyte membrane deformation is certainly best characterized as occurring at constant area, accommodated by an arbitrary variation in interfacial tension, whereas in our drop model, interfacial tension is constant. An improved model, which retains the advantages we note above, might be produced by postulating an interfacial tension which depends upon local interface curvature and imposing the constraint of constant surface area. We have these developments in hand: meanwhile, the implicit assumption which is made in this work is that, in the absence of strong shape perturbations, membrane elasticity may be adequately approximated by interfacial tension.

The regular lattice, single relaxation-time multi-component LB simulation used [36] in this section may be classified D2Q9 LBGK [17]. For all results reported in this section, the wavelength, λ, of the wavy-wall was resolved on 300 regular lattice sites, giving a spatial resolution $\Delta x \equiv \lambda/300 = 15 \times 10^{-6}/300 = 5 \times 10^{-8}$ m. The plasma fluid component was represented by LB relaxation parameter, $\omega = 1/\tau$ (see Eq. (1)) given by $\omega = 0.8$, and the drop fluid by $\omega = 0.174$ (consistent with a viscosity contrast of 7). Equilibrated flows were defined to have (i) equi-spaced particles, all with their centre close to the horizontal axis of symmetry and (ii) a velocity residual characterized by a single time constant, $T_0 = \lambda/\langle u_d \rangle$, corresponding to one erythrocyte "transit" over one wavy wall wavelength, λ. Here $\langle u_d \rangle$ is the time-averaged drop drift velocity. The Reynolds number, now defined as:

$$\mathrm{Re} = \frac{\rho \langle u_d \rangle H}{\mu},$$

with $H = 2\lambda/3$ the channel half-width, had a value close to unity. Note that this definition of Re differs slightly from that used in the previous section. The instantaneous WSS distribution at the wavy-wall surface was measured at regular time intervals during one particle transit, at all 300 distinct grid positions. Fig. 8 shows, for all spatial positions on the wavy-wall, the temporal maximum, minimum and mean WSS values, normalized to their spatial-temporal maximum value WSS_0, measured without any particles present, i.e. at 0% hematocrit. We note that, within the present, albeit very limited context, with a low hematocrit, the evident correspondence between the erythrocyte transit time averaged, mean WSS (diagonal crosses) and the 0% hematocrit value (broken line) clearly

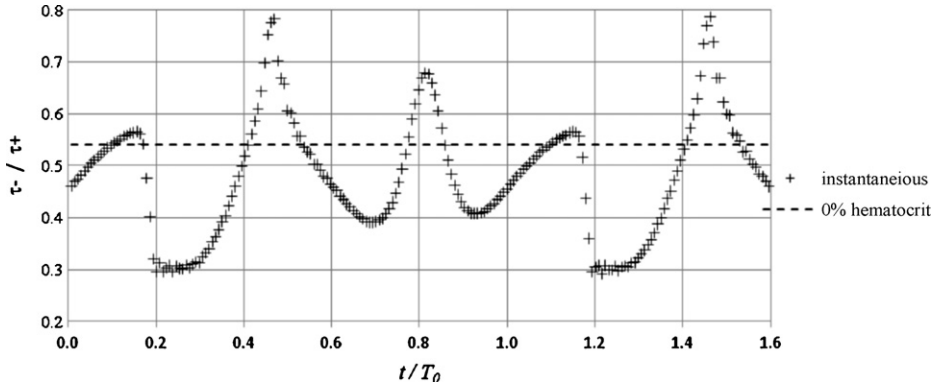

Fig. 9. The time-variation of the instantaneous WSS ratio, τ_-/τ_+ (crosses). The broken line corresponds to the constant value of $\tau_-/\tau_+ \approx 0.55$ characteristic of the continuum. This modality of WSS cannot be recovered by an incompressible, Newtonian fluid approximation.

supports a view of continuum haemadynamics as a "mean value" regime, even at the present scale. Notwithstanding the previous remark, we note the very large fractional fluctuations in WSS apparent in Fig. 9, which assesses the time-variation of the instantaneous WSS ratio, τ_-/τ_+. Recall, $\tau_-(\tau_+)$ is measured at location $x = 0$ ($x = \lambda/2$), corresponding to the valley (peak) of the wavy-wall. Note that this modality of WSS cannot be recovered by an incompressible Newtonian fluid approximation alone. To underscore this point, the broken horizontal line in Fig. 9 corresponds to value of $\tau_-/\tau_+ = 0.55$ typical of our continuum calculations. The time-averaged, mean value of the ratio τ_-/τ_+ was computed, by numerical integration, to be approximately 0.4857.

7. Concluding remarks

While atheroma are pathologically associated with larger arteries, the high sensitivity of wall shear stress to the wall undulation supports the hypothesis that the likely onset of clinical changes at the artery wall also occurs in small arteries, of which remodelling is a possibility. However, the endothelial surface is not only wavy in its geometry, but, at lower scale, it is covered by a ciliate layer called *glycocalyx* (or ESL) [40], one of the functions of which is to provide protection to the endothelium. The remodelling may occur particularly in more progressed stages of the disease when the protective layer of the glycocalyx has been damaged or is no longer present. Then the endothelium becomes directly exposed to the flow, a condition consistent with the current model. Fig. 8 suggests that the erythrocyte transit time-averaged WSS spatial distributions largely conform with the predictions of continuum hydrodynamics. However, Fig. 9 underscores the need to consider the particulate nature of blood, as a suspension of deformable particles. In more detail, critical flow regions, such as low WSS, rapidly varying WSS sites or, in extreme cases, turbulence regions, are assumed to stimulate the glycocalyx to send biochemical signals for the formation of fatty structures, such as atherosclerotic plaque. Recently, some mathematical modelling work has been carried out by Arslan [41] and Vincent et al. [42], using a porous medium to model the glycocalyx layer. However, none of these works includes the effect of the roughness of the wall, which should be added for a realistic description that encompasses the fluctuating WSS considered in Sections 5 and 6. The presence of glycocalyx alters the boundary condition of the problem, in particular the classical no-slip condition at the vessel wall may have to be replaced to allow for plasma penetration through it. In turn, this may lead to significant changes in the predicted pressure drop and possibly to a smoothing of such fluctuations, as identified in Section 6. A detailed discussion of models at scales smaller than 10 μm is beyond the scope of the present work. Since, however, an analysis of the extended corrugation/glycocalyx model is feasible, it will form an objective of future investigations.

Conflict of interest statement

The authors disclose any financial and personal relationships with other people or organisations that could inappropriately influence (bias) this work.

References

[1] Nerem RM. Vascular fluid mechanics, the arterial wall, and atherosclerosis. J Biomech Eng 1992;114(3):274–83.
[2] Caro CG. Discovery of the role of wall shear in atherosclerosis. Arterioscl Thromb Vasc Biol 2009;29:158–61.
[3] Shimogonya Y, Ishikawa T, Imai Y, Matsuki N, Yamaguchi T. Can temporal fluctuation in spatial wall shear stress gradient initiate a cerebral aneurysm? A proposed novel hemodynamic index, the gradient oscillatory number (GON). J Biomech 2009;42:550–4.
[4] Caro CG, Fitz-Gerald JM, Schroter RC. Atheroma and arterial wall shear: observation, correlation and proposal of a shear dependent mass transfer mechanism for atherogenesis. Proc R Soc Lond B 1971;177:109–59.
[5] Malek AM, Alper SL, Izumo S. Hemodynamic shear stress and its role in atherosclerosis. JAMA 1999;282:2035–42.
[6] Sato M, Ohashi T. Biorheological views of endothelial cell responses to mechanical stimuli. Biorheology 2005;42:421–41.
[7] Punchard MA, Stenson-Cox C, O'Cearbhaill ED, Lyons E, Gundy S, Murphy L, et al. Endothelial cell response to biomechanical forces under simulated vascular loading conditions. J Biomech 2007;40:3146–54.
[8] Satcher RL, Bussolari SR, Gimbrone MA, Dewey CF. The distribution of fluid forces on model arterial endothelium using computational fluid dynamics. J Biomech Eng 1992;114:309–16.
[9] Tsangaris S, Leiter E. On laminar steady flow in sinusoidal channels. J Eng Math 1984;18:89–103.
[10] Sobey IJ. Flow through furrowed channels. Part I. Calculated flow patterns. J Fluid Mech 1980;96:1–26.
[11] Kaliakatsos Ch, Pentaris A, Koutsouris D, Tsangaris S. Application of an artificial compressibility methodology for the incompressible flow through a wavy channel. Commun Numer Meth Eng 1996;12:359–69.
[12] Luo H, Pozrikidis C. Shear-driven and channel flow of a liquid film over a corrugated or indented wall. J Fluid Mech 2006;556:167–88.
[13] Wang HL, Wang Y. Flow in microchannels with rough walls: flow pattern and pressure drop. J Micromech Microeng 2007;17:576–96.
[14] Focke WW, Knibbe PG. Flow visualization in parallel-plate ducts with corrugated walls. J Fluid Mech 1986;165:73–7.
[15] Nishimura T, Murakami S, Arakawa S, Kawamura Y. Flow observations and mass transfer characteristics in symmetrical wavy-walled channels at moderate Reynolds numbers for steady flows. Int J Heat Mass Transf 1990;33(5):835–45.
[16] Weinbaum S, Zhang X, Han Y, Vink H, Cowin SC. Mechanotransduction and flow across the endothelial glycocalyx. PNAS 2003;100(13):7988–95.
[17] Succi S. The lattice Boltzmann equation for fluid dynamics and beyond. Oxford: Oxford University Press; 2001.
[18] Amati G, Succi S, Piva R. Massively parallel Lattice-Boltzmann simulation of turbulent channel flow. Int J Mod Phys C 1997;8:869–77.
[19] Desplat JC, Pagonabarraga I, Bladon P. LUDWIG: a parallel lattice-Boltzmann code for complex fluids. Comput Phys Commun 2001;134:273–90.
[20] Fyta M, Melchionna S, Kaxiras E, Succi S. Multiscale coupling of molecular dynamics and hydrodynamics: application to DNA translocation. Multi Model Simul 2006;5:1156–73.
[21] Mazzeo M, Coveney PV. HemeLB: A high performance parallel lattice-Boltzmann code for large scale fluid flow in complex geometries. Comput Phys Commun 2008;178:894–914.
[22] Artoli AM, Hoekstra AG, Sloot PMA. Mesoscopic simulations of systolic flow in the human abdominal aorta. J Biomech 2006;39:873–84.
[23] Bernaschi M, Melchionna S, Succi S, Fyta M, Kaxiras E, Sircar J. MUPHY: a parallel multiphysics/scale code for high-performance bio-fluidic simulations. Comput Phys Commun 2009;180:1495–502.
[24] Guo Z, Zheng C, Shu B. Discrete lattice effects on the forcing term in the lattice Boltzmann method. Phys Rev E 2002;65:046308.
[25] Peng G, Xi H, Duncan C. Lattice Boltzmann method on irregular meshes. Phys Rev E 1998;58:R4124.
[26] Ubertini S, Succi S, Bella G. Lattice Boltzmann schemes without coordinates. Phil Trans R Soc Lond A 2004;362:1763–71.
[27] Janela J, Sequeira A, Pontrelli G, Succi S, Ubertini S. Unstructured Lattice-Boltzmann method for hemodynamic flows with shear-dependent viscosity. Int J Mod Phys C 2010;21(6):1–17.
[28] Reichlin T, Wild A, Dürrenberger M, Daniels AU, Aebi U, Hunziker PR, et al. Investigating native coronary artery endothelium in situ and in cell culture by scanning force microscopy. J Struct Biol 2005;152:52–63.
[29] König CS, Long Q, Collins MW, Xu S. Numerical assessment of wall shear stress along the endothelial surface layer in small arteries. The vascular endothelium, basic and clinical aspects, 6th international congress. Abstract Biomed Pharmacother 2006;60:480–7.
[30] Safar ME. Peripheral pulse pressure, large arteries, and microvessels. Hypertension 2004;44:121–2.
[31] Benzi R, Succi S, Vergassola M. The Lattice Boltzmann equation: theory and applications. Phys Rep 1992;222:145–97.
[32] Secomb TW, Hsu R. Resistance to blood flow in non-uniform capillaries. Microcirculation 1997;4:421–7.
[33] Secomb TW, Hsu R, Pries AR. Blood flow and red blood cell deformation in nonuniform capillaries: effects of the endothelial surface layer. Microcirculation 2002;9:189–96.
[34] Dupin MM, Halliday I, Care CM, Munn L. Modeling the flow of dense suspensions of deformable particles in three dimensions. Phys Rev E 2007;75:066707.
[35] Hollis AP, Halliday I, Care CM. An accurate and versatile lattice closure scheme for lattice Boltzmann equation fluids under external forces. J Comput Phys 2008;227:8065–82.
[36] Halliday I, Hollis AP, Care CM. Lattice Boltzmann algorithm for continuum multicomponent flow. Phys Rev E 2007;76:026708.
[37] Bouzidi M, Firdaouss M, Lallemand P. Momentum transfer of a Boltzmann-lattice fluid with boundaries. Phys Fluids 2001;13(11):3452–9.
[38] Kim SH, Pitsch H. A generalized periodic boundary condition for lattice Boltzmann method simulation of a pressure driven flow in a periodic geometry. Phys Fluids 2007;19:108101.

[39] Halliday I, Spencer TJ, Care CM. Validation of multicomponent lattice Boltzmann equation simulations using theoretical calculations of immiscible drop shape. Phys Rev E 2009;79:016706.
[40] Weinbaum S, Tarbell JM, Damiano ER. The structure and the function of the endothelial glycocalyx layer. Annu Rev Biomed Eng 2007;9:6.1.
[41] Arslan N. Mathematical solution of the flow field over glycocalyx inside vascular system. Math Comp Appl 2007;12(3):173–9.
[42] Vincent PE, Sherwin SJ, Weinberg PD. Viscous flow over outflow slits covered by an anisotropic Brinkman medium: a model of flow above interendothelial cell cleft. Phys Fluids 2008;20(6):063106.